

Discriminating Seagrasses From Green Macroalgae in European Intertidal areas using high resolution multispectral drone imagery

Simon Oiry

Bede Ffinian Rowe Davies

Ana I. Sousa

Philippe Rosa

Maria Laura Zoffoli

Guillaume Brunier

Pierre Gernez

Laurent Barillé

2024-10-14

Abstract

Coastal areas support seagrass meadows, which offer crucial ecosystem services including erosion control and carbon sequestration. However, these areas are increasingly impacted by human activities, leading to habitat fragmentation and seagrass decline. In situ surveys, traditionally

performed to monitor these ecosystems face limitations on temporal and spatial coverage, particularly in intertidal zones, prompting the addition of satellite data within monitoring programs. Yet, satellite remote sensing can be limited by too coarse spatial and/or spectral resolution, making it difficult to discriminate seagrass from other macrophytes in highly heterogeneous meadows. Drone (unmanned aerial vehicles – UAV) images at a very high spatial resolution offer a promising solution to address challenges related to spatial heterogeneity and intrapixel mixture. This study focuses on using drone acquisitions with a ten spectral band sensor similar to that onboard Sentinel-2, for mapping intertidal macrophytes at low tide (i.e. during a period of emersion) and effectively discriminating between seagrass and green macroalgae. Nine drone flights were conducted at two different altitudes (12 m and 120 m) across heterogeneous intertidal European habitats in France and Portugal, providing multispectral reflectance observation at very high spatial resolution (8 mm and 80 mm respectively). Taking advantage of their extremely high spatial resolution; the low altitude flights were used to train a Neural Network classifier to discriminate five taxonomic classes of intertidal vegetation: Magnoliopsida (Seagrass), Chlorophyceae (Green macroalgae), Phaeophyceae (Brown algae), Rhodophyceae (Red macroalgae) and benthic Bacillariophyceae (Diatoms), and validated using concomitant field measurements. Classification of drone imagery resulted in an overall accuracy of 94% across all sites and images, covering a total area of 467 000 m². The model exhibited an accuracy of 96.4% in identifying seagrass. In particular, seagrass and green algae can be discriminated. The very high spatial resolution of the drone data made it possible to assess the influence of spatial resolution on the classification outputs, showing a limited loss in seagrass detection up to about 10m. Altogether, our findings suggest that the Multi-Spectral Instrument (MSI) onboard Sentinel-2 offers a relevant

trade-off between its spatial and spectral resolution, thus offering promising perspectives for satellite remote sensing of intertidal biodiversity over larger scales.

1. Introduction

Coastal areas are vital hotspots for marine biodiversity, with intertidal seagrass meadows playing a crucial role at the interface between land and ocean (Unsworth et al., 2022). Seagrass meadows provide a myriad of ecosystem services, including carbon sequestration, oxygen production, protection against sea-level rise and coastline erosion, and mitigation of eutrophication (Sousa et al., 2019; Unsworth et al., 2022). They serve as vital habitats for a diverse array of marine and terrestrial species, providing living, breeding, and feeding grounds (Gardner and Finlayson, 2018; Jankowska et al., 2019; Zoffoli et al., 2022). Due to the concentration of human activities in coastal zones, seagrass meadows are directly exposed to and impacted by anthropogenic pressures. Global regression and fragmentation of seagrass meadows are currently observed due to climate change, diseases, urbanization, land reclamation, dredging, competition with alien species, and reduction in water quality (Chefaoui et al., 2018; Duffy et al., 2019; Lin et al., 2018; Nguyen et al., 2021; Orth et al., 2006; Rasheed and Unsworth, 2011; Soissons et al., 2018; Sousa et al., 2019). Both habitat fragmentation and reduction, in turn, can severely compromise the effectiveness of ecosystem services provided by seagrass meadows. While improvements in water quality and hydrodynamics have been recently reported in Europe, allowing an overall recovery of seagrass ecosystems at local and European scales, many coastal waters worldwide are still subjected to strong eutrophication processes (Los Santos et al., 2019; Sousa et al., 2019; Zoffoli et al., 2021). Coastal eutrophication has been associated with excessive accumulation of green macroalgae, so-called green tides (Devlin and Brodie, 2023). Green tides produce shade and suffocation over seagrass individuals, thus threatening the health of seagrass ecosystems (Wang et al., 2022).

The importance of seagrass meadows and the variety of ecosystem services they provide have led to the enhancement of both global and regional programs to monitor Essential Oceanic Variable (EOVs) such as seagrass composition (Miloslavich et al., 2018), as well as Essential Biodiversity Variable (EBVs) such as seagrass taxonomic diversity, species distribution, population abundance, and phenology (Pereira et al., 2013). Traditionally, indicators of seagrass status have been quantified using *in situ* measurements. However, the acquisition of field measurements in intertidal zones is notoriously challenging. Intertidal seagrass meadows are only exposed during low tide and can be situated in difficult-to-reach mudflats, potentially leading to inaccurate and limited estimations with conventional sampling techniques (Nijland et al., 2019). Satellite observations have been proven effective in complementing *in situ* sampling, allowing for near real-time and consistent retrieval of seagrass EOVs and EBVs over extensive meadows (Coffer et al., 2023; Davies et al., 2024a, 2024b; Traganos and Reinartz, 2018; Xu et al., 2021; Zoffoli et al., 2021).

While satellite remote sensing (RS) provides temporally consistent observations over large spatial scales, its utilization over intertidal areas is limited by several constraints. Satellite missions with a high temporal resolution (e.g. daily MODIS observation) are limited by too coarse spatial resolution (>100 m) to accurately map patchy seagrass meadows. Missions with a high spatial resolution such as Sentinel-2 (10 m) or Landsat8/9 (30 m) can be limited by low spectral resolution. The limited number of spectral bands challenges accurate discrimination of seagrass from other co-existing macrophytes. In particular, Chlorophyceae (green algae) and marine Magnoliopsida (seagrass) share the same pigment composition (Douay et al., 2022; Ralph et al., 2002), resulting in a similar spectral signature in terms of reflectance, especially in the visible range (Bannari et al., 2022; Davies et al., 2023a). Recently, using advanced machine-learning algorithms trained with a large hyperspectral library of more than 300 field reflectance spectra, Davies et al. (2023a) demonstrated that it was possible to discriminate Magnoliopsida from Chlorophyceae using reflectance spectra at Sentinel-2's spectral resolution. However, the application of this approach to satellite RS remains to be validated. Moreover, patches of green algae can develop at small

spatial scales that are not observable using Sentinel-2 and/or Landsat-8/9 images (Tuya et al., 2013), especially during the initial stage of a green tide.

Drones (Unmanned Aerial Vehicles – UAVs) can potentially fill the data gaps left by satellite RS and *in situ* measurements, due to their ability to provide spatially-explicit observations at very high spatial resolutions (pixel size from mm to cm) while capturing data at multi-spectral resolution (Fairley et al., 2022; Oh et al., 2017). The versatility of drones allows for their application across a diverse thematic range, from coastal zone management (Adade et al., 2021; Angnuureng et al., 2022; Casella et al., 2020) to mapping species distribution (Brunier et al., 2022; Joyce et al., 2023; Roca et al., 2022; Román et al., 2021; Sousa et al., 2019; Tallam et al., 2023). However, when applied to coastal habitat mapping, previous case studies were mostly limited to a low number of flights over a single study site, restricting the generalizability of their application over wider geographical scales (Brunier et al., 2022; Collin et al., 2019; Román et al., 2021; Rossiter et al., 2020). The present study aimed at analyzing the potential of multispectral drone RS to map intertidal macrophytes over a diverse biogeographical range, with a particular focus on discriminating Magnoliopsida and Chlorophyceae (Seagrass and Green Algae, respectively). Nine drone flights were performed over soft-bottom intertidal areas along the Atlantic coastlines of two European countries (France and Portugal), covering a wide range of habitats, from monospecific seagrass meadows to meadows mixed with green, or red macroalgae. A deep learning algorithm was trained and validated for macrophyte discrimination, emphasizing applicability across diverse sites without a loss of prediction accuracy. The classification maps obtained at a very high spatial resolution with the drone were spatially degraded to satellite resolutions, making it possible to assess the effect of spatial resolution on classification accuracy, and provide insights for coastal habitat mapping using satellite remote sensing.

106 **2. Material & Methods**

107 **2.1 Study sites**

108 Seven study sites distributed between France and Portugal were selected for their extensive intertidal
109 seagrass beds. Two sites were located in the Gulf of Morbihan, France (Figure 1 A : 47.5791°N, 2.8018°W).
110 This gulf covers an area of 115 km² and is only connected to the sea through a 900 m wide channel. A total
111 of 53 small islands are scattered across the gulf leading to 250 km of shorelines. Patchy seagrass meadows
112 can be found on many of these islands. One of the sites within the gulf was on one of its islands (Arz) and
113 the other was located further south on a mainland beach area (Duer). The Gulf of Morbihan is a Natura
114 2000 site and a Regional Protected Area due to its rich biodiversity, including its seagrass meadows, and is
115 also classified as a RAMSAR site, which highlights its significance as a wetland of international
116 importance. Two other sites were located in Bourgneuf Bay, France (Figure 1 B : 46.9849°N, 2.1488°W)
117 which is a 340 km² semi-enclosed macrotidal bay, protected from waves by Noirmoutier Island. Bourgneuf
118 bay hosts a large intertidal seagrass meadow of about 6 km² (Zoffoli et al., 2020). Within this meadow, the
119 sites observed by drones (L'Epine and Barbatre) contained monospecific beds of *Nanozostera noltei* (dwarf
120 eelgrass, syn. *Zostera noltei*) with very little mixing with other macrophytes. Bourgneuf Bay is also part of
121 the Natura 2000 network and serves as a RAMSAR site due to its critical habitat for migratory bird species
122 and its extensive seagrass meadows (Zoffoli et al., 2022). Three sites were surveyed in the Ria de Aveiro
123 Coastal Lagoon in Portugal (Figure 1 C : 40.6887°N, 8.6810°W). The extent of this lagoon is ~83 km² (at
124 low tide) with many narrow channels, large salt marshes and many mudflats that uncover at low tide (Sousa
125 et al., 2017). It is connected to the open sea through a single channel, with a tidal lag between the North
126 and the South of the lagoon. The southernmost site (Gafanha) is a mudflat located in the Mira channel (one
127 of the four main channels of the lagoon) whereas the two other sites (Mataducos and Marinha Lanzarote)
128 were situated in the middle of the lagoon and only accessible by boat. These Portuguese sites are
129 characterized by a more diverse intertidal vegetation, where patches of seagrass intermingle with red,

130 brown, and green macroalgae. The Aveiro Lagoon, like the other study areas, is a Natura 2000 site and a
 131 RAMSAR wetland, recognized for its rich mosaic of habitats and importance for biodiversity, including
 132 migratory bird species and intertidal vegetation.

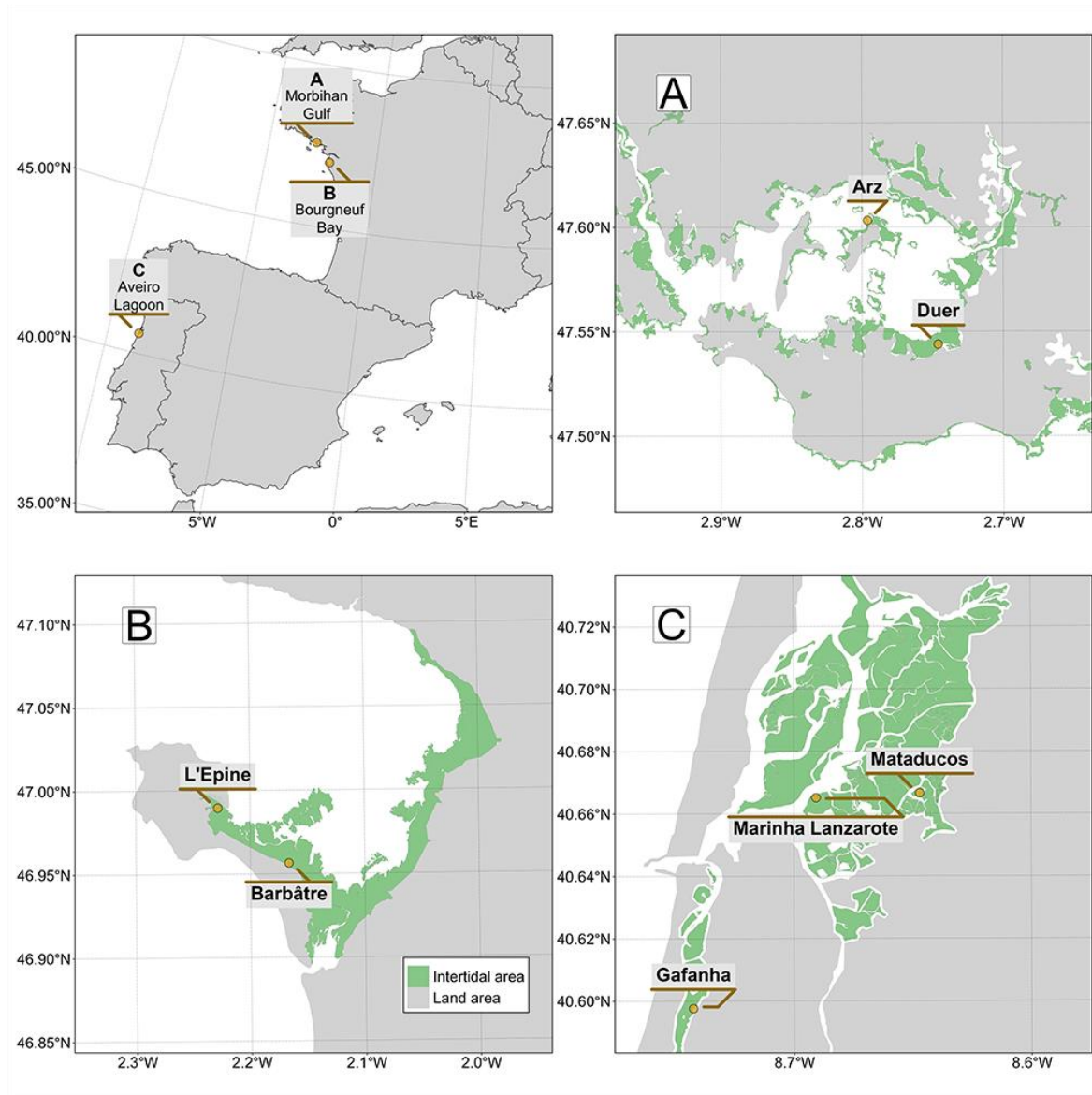


Figure 1: Location of drone flights in France and Portugal. A: Gulf of Morbihan (Two sites), B: Bourgneuf Bay (Two sites), C: Ria de Aveiro Coastal Lagoon (Three sites). Green areas represent the intertidal zone.

2.2 Field sampling

2.2.1 Drone acquisition

At each location, a DJI Matrice 200 quadcopter drone equipped with a Micasense RedEdge Dual MX multispectral camera was flown to take 1.2 million pixel reflectance photographs with ten spectral bands ranging from the blue to the near infrared (NIR): 444, 475, 531, 560, 650, 668, 705, 717, 740 and 840 nm. To ensure consistent lighting conditions across flight paths, the drone's trajectory was aligned to maintain a solar azimuth angle of 90 degrees. An overlap of 70% and 80% (side and front respectively) between each image was set for each flight. A downwelling light sensor (DLS2) was used to acquire irradiance data concomitantly with the camera measurements. Raw data were calibrated in reflectance using a calibration panel reflective at ~50% provided by the manufacturer. Across all sites, flights were made at two different altitudes : 12 m or/and 120 m, with a spatial resolution of 8 mm and 80 mm, respectively (Table 1).

Table 1: List of drone flights, summarizing the date, the altitude, and the purpose of each flight. 12 m and 120 m flights have a spatial resolution of 8 and 80 mm respectively.

Country	Site	Name	Altitude	Utility	Date
France	Gulf of Morbihan	Arz Island	12m	Training	29/09/2022
		Duer	12m	Training	14/07/2022
		Duer	120m	Validation	14/07/2022
	Bourgneuf Bay	Barbâtre	120m	Validation	07/09/2021
		L'Epine	120m	Validation	08/07/2021
Portugal	Aveiro Lagoon	Marinha Lanzarote	120m	Validation	17/06/2022
		Mataducos	120m	Validation	16/06/2022
		Gafanha	120m	Validation	15/06/2022
		Gafanha	12m	Training	15/06/2022

144 2.2.2 Ground Control Points

145 Before each flight, targets used as ground control points were distributed over the study site and
146 georeferenced with a Trimble © Geo XH 6000 differential GPS (dGPS). Ground control points were used
147 to correct georeferencing imprecision of orthomosaics with a horizontal and vertical accuracy of 10cm. A
148 dGPS was also used to georeference quadrats of 0.25 m², which assessed the presence or absence of five
149 key taxonomic classes of intertidal vegetation : Bacillariophyceae (unicellular benthic diatoms forming
150 biofilms at the sediment surface during low tide), Phaeophyceae (brown macroalgae), Magnoliopsida
151 (dwarf eelgrass), Chlorophyceae (green macroalgae) and Rhodophyceae (red macroalgae) (Figure 2). Only
152 homogeneous vegetation patches extending over several meters were selected as ground control points.
153 Pictures of each quadrat were uploaded online to the open-portal Global Biodiversity Information Facility
154 (GBIF) platform (Davies et al., 2023b). Each photograph was also processed to estimate the percent cover
155 of each type of vegetation using an image processing software (ImageJ, Schneider et al., 2012).
156 Hyperspectral reflectance signatures of each vegetation class were recorded using an ASD FieldSpec
157 HandHeld 2 spectroradiometer, which acquires reflectance between 325 and 1075 nm, with 1 nm of spectral
158 resolution. Hyperspectral signatures served dual purposes: they validate the radiometric calibration of drone
159 data and contribute to misclassification reduction in photo interpretations.

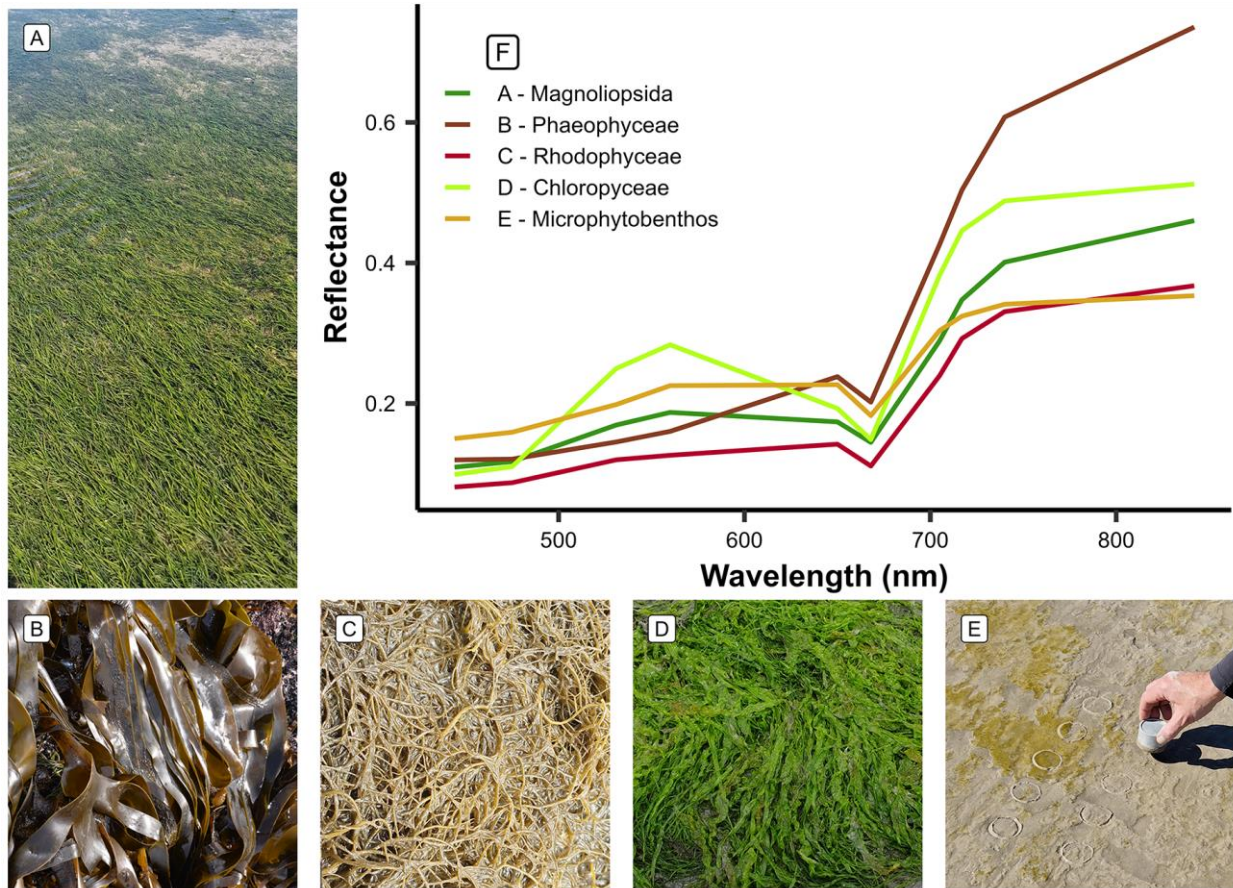


Figure 2: The five taxonomic classes of vegetation used to train the Neural Network model and their raw spectral signatures at the spectral resolution of the Micasense RedEdge Dual MX. A: Magnoliopsida (*Nanozostera noltei* syn. *Zostera noltei*); B: Phaeophyceae (*Fucus* sp.); C: Rhodophyceae (*Gracilaria vermiculophylla*); D: Chlorophyceae (*Ulva* sp.); E: Bacillariophyceae (Diatoms - MPB)

2.3 Drone Processing

A structure-from-motion photogrammetry software (Agisoft Metashape, Agisoft, 2019) was used to process images to obtain multispectral orthomosaics of each flight. The process of orthomosaicking was identical for every flight. First, key tying points were detected inside of each image and between overlapping images

in order to obtain a sparse point cloud. This cloud was cleaned using a reprojection accuracy metric in order to remove noisy points. A dense point cloud was then produced using a structure from motion algorithm. A surface interpolation of this dense point cloud was made to obtain a digital surface model (DSM), used to reconstruct the multispectral ortho-image (Nebel et al., 2020). Low altitude drone flights produced ortho-images with a very high spatial resolution (8 mm per pixel), making it efficient to visually distinguish between the various types of vegetation. High altitude flights allowed to cover larger areas and produced images with a pixel size of 80 mm (Table 1).

2.4 General Workflow

The spectral similarities of the reflectance signatures at the spectral resolution of the micasense sensor between intertidal green macrophytes (Magnoliopsida and Chlorophyceae) make their discrimination challenging using simple classification algorithms (Figure 2 F). To overcome this challenge, a deep learning classification method was trained, validated, and applied to each drone flight (Figure 3).

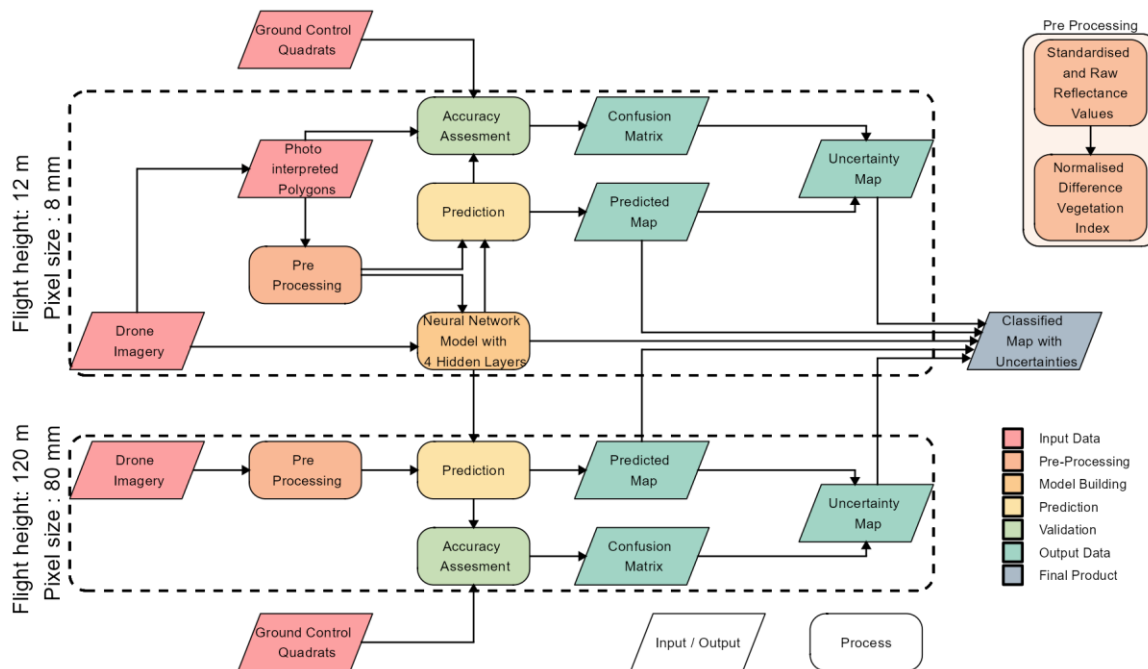


Figure 3: Schematic representation of the workflow. Parallelograms represent input or output data, and rectangles represent Python processing algorithms. The overall workflow of this study is divided into two distinct parts based on the spatial resolution of the drone flights: high-resolution flights (pixel size: 8 mm) were utilized for training and prediction of the Neural Network model, whereas lower-resolution flights (pixel size: 80 mm) were solely employed for prediction purposes. Validation has been performed on both high- and low-resolution flights.

2.4.1 Training dataset building

Table 2: Vegetation Classes of the model and the number of pixels used to train and validate each class.

Class	Training Pixels	Validation Pixels
Bacillariophyceae	4,475	9,807
Chlorophyceae	17,140	25,910
Magnoliopsida	221,065	179,119
Phaeophyceae	169,936	82,161
Rhodophyceae	5,771	10,054

A dataset containing photo-interpreted drone reflectance pixels was built to train a Neural Network model. The training pixels were categorized into seven different classes, representing the various habitats encountered at the different study sites: Sediment, Water, Chlorophyceae, Magnoliopsida, Bacillariophyceae, Phaeophyceae and Rhodophyceae. Only data from the low-altitude flights (Table 1) were used for training because their 8 mm spatial resolution allowed to avoid spectral sub-pixel mixing and to accurately identify vegetation classes. More than 418,000 pixels at 8 mm resolution from the 3 training

flights were used to train the model (Table 2). Twenty one variables were used by the model as predictors: the ten raw spectral bands of the Micasense RedEdge Dual MX multispectral camera (ranging from 444 nm to 840 nm), the same ten spectral bands standardized using a min/max transformation (Equation 1 ; Cao et al. (2017)) and the Normalized difference vegetation index (NDVI, Equation 2). Standardisation of spectral bands is commonly used to eliminate the scaling differences between spectra and to limit the effect of biomass on the spectra shape (Davies et al., 2023a; Douay et al., 2022).

$$R_i^*(\lambda) = \frac{R_i(\lambda) - \min(R_i)}{\max(R_i) - \min(R_i)} \quad (1)$$

where $R_i(\lambda)$ is the reflectance at the wavelength (λ) of each individual spectra (i), $\min(R_i)$, and $\max(R_i)$ are the minimum and maximum value of the spectra (i)

$$NDVI = \frac{R(840nm) - R(668nm)}{R(840nm) + R(668nm)} \quad (2)$$

where $R(840nm)$ is the reflectance at 840 nm and $R(668nm)$ is the reflectance at 668 nm.

2.4.2 Model building

A neural network classification model was built using the fastai workflow (Howard et al., 2018). This model was composed of 2 hidden layers and has a total of 26 054 trainable parameters. Parameters have been fine tuned using 12 epoch to minimize the error rate. This model has been called DISCOV, standing for Drone Intertidal Substrat Classification Of Vegetation.

2.4.3 Validation

The workflow of this study revolves around two distinct flight heights (12 and 120 m, Figure 3) where ensuring consistency between reflectances at both heights is crucial. This comparison was conducted at sites where low and high-altitude flights overlapped. The low altitude flights were resampled to the same spatial resolution and grid as the high flights using a median resampling method. Reflectance values were

then extracted, and a scatterplot was generated, and the Root Mean Square Error (RMSE) was computed to compare the difference between the raw and standardised reflectance.

The classification model was applied to all flights at both 12 and 120 m of altitude. *In situ* information on georeferenced class type and percent cover, acquired over homogeneous vegetation patches at the same time as drone flights was used to assess the model accuracy. These images were used to construct a validation dataset indicating the presence or absence of each class. Additionally, to the quadrat-based validation dataset, polygons of each class were photo interpreted in order to increase the number of pixels of the validation dataset. A total of 536,000 pixels were used to validate the Neural Network classifier. The sites with the lowest and highest number of validation data were Gafanha Low (17316 pixels) and Marinha Lanzarote (159713 pixels), respectively. A confusion matrix, along with precision metrics such as global accuracy, sensitivity, specificity, F1 score, and Kappa coefficient, were generated for each site. All validation matrices were then aggregated to create an overall matrix.

2.5 Variable Importance

Variable Importance Plots (VIP) serve as a method to identify which predictors are important for predicting a specific class. Out of the 21 predictors utilized in this study, Variable Importance was computed only for the raw and standardized values of the 10 spectral bands captured by the MicaSense camera. This is achieved by repeatedly predicting the same dataset while randomly shuffling one predictor at a time. The benchmark score obtained after each iteration is then compared to the benchmark score obtained without shuffling any variables. The greater the difference between these two benchmark values, the more important the variable is for the model (Wei et al., 2015).

2.6 Influence of the spatial resolution on classification

To evaluate the influence of spatial resolution on the model's output, we resampled the drone orthomosaics from their native resolution (8 cm for the high altitude flights) using the "average" method from the Terra

package in R. DISCOV was then applied to these resampled rasters, and the results were compared to the original model predictions. For each resolution and vegetation class, we calculated the predicted area loss, where a score of 0 indicates no area loss during spatial resampling, and a score of 100 indicates complete loss of the vegetation class.

We used a Generalized Linear Model (GLM) with a Beta distribution to examine the relationship between pixel resolution, vegetation class, and their interaction on the loss of vegetation. The loss of vegetation was modelled as a function of the interaction between pixel resolution and vegetation class (Bacillariophyceae, Phaeophyceae, Magnoliopsida, Chlorophyceae and Rhodophyceae). Sample vs fitted residuals and quartile-quartile graphics were assessed visually, to ensure assumption of the models used were met.

2.7 Impact of mixed vegetation cover on the prediction

The key aspect of the workflow adopted in the present study is the mapping at two different altitudes (12 and 120 m), resulting in two distinct resolutions for the same area (8 and 80 mm; respectively). The high-resolution flight was used to estimate the sub-pixel composition for each pixel of the lower-resolution flight. Consequently, within each pixel of the high-altitude flights, the contribution of each vegetation class (% cover) was obtained, and a kernel density plot was generated. This plot provided a visual representation of the model's behavior in mixed vegetation scenarios. It helps to understand the minimum vegetation cover of a given class within a pixel necessary for the model to confidently predict that class.

3. Results

3.1 Reflectance comparison between the two different altitudes

In this study, drone flights were conducted at two different altitudes (12 and 120 m) to construct the neural network model. At the sites where the flights at both altitudes overlapped, reflectance was compared. Overall, there was a good agreement between the two altitudes (RMSE: 0.027; Figure 4).

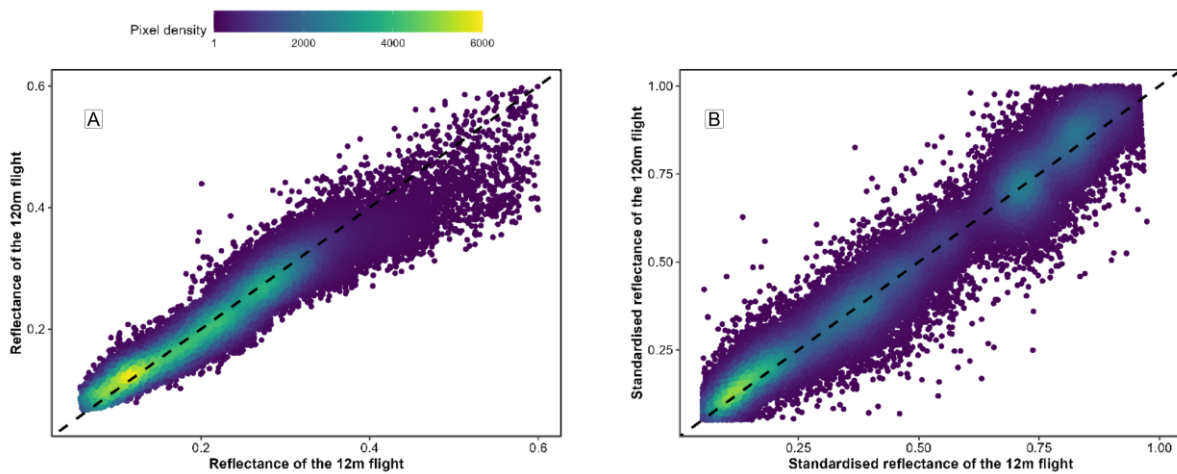


Figure 4: Comparison of reflectance retrieved from both low-altitude and high-altitude flights over a common area. The black dashed line represents a 1 to 1 relationship. Left (A) plots raw data and right (B) plots standardized data (Equation 1).

There was a slight underestimation for raw reflectance values in the high-altitude flight, particularly for higher reflectance values (Figure 4 A). Since both flights were conducted over vegetated areas, the highest reflectance values correspond to the infrared part of the spectrum. This difference was not present when the reflectance has been standardized (Equation 1 ; Figure 4 B).

3.2 Classification

Each drone flight was used to produce a prediction map, as well as a probability map that indicates the model derived probability of the selected class for every pixel. The low-altitude flight conducted in Gafanha, Portugal, represented the site with the highest complexity (Figure 5). Among the five vegetation classes on which the model was trained, four were present on this site, with green and red macroalgae mixed with a seagrass meadow. There were also diatoms forming biofilms on bare sediment surface. Although the seagrass was solely composed of a single species, *Nanozostera noltei*, various colors of this species could be observed from dark green (corresponding to healthy leaves) to brown (when leaves are senescent or have an altered pigment composition). Regardless of the variation of color, the class Magnoliopsida was accurately predicted by the model (F1 score of 0.96 at that site).

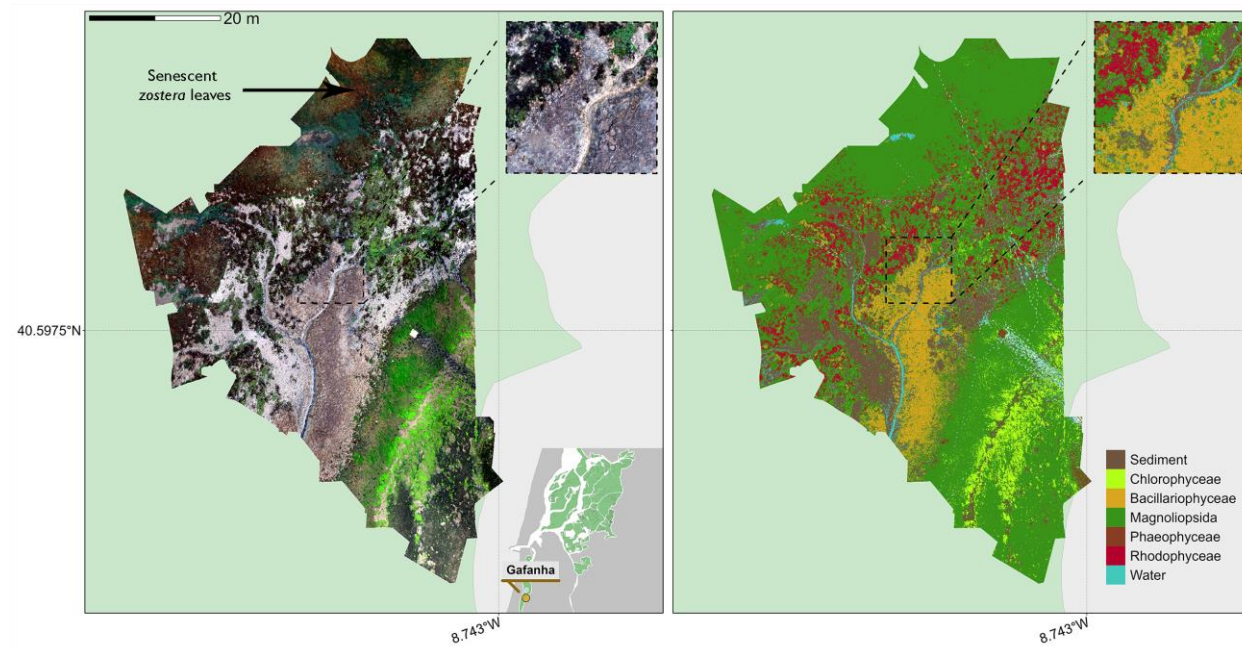


Figure 5: RGB orthomosaic (Left) and Prediction (Right) of the low altitude flight of Gafanha, Portugal. The total extent of this flight was 3000 m² with a resolution of 8 mm per pixel.

Background colors indicate intertidal area (Light Green) and land area (Light Grey). The zoom covers an area equivalent to a 10-meter Sentinel-2 pixel size.

263 The high-altitude flight over Gafanha covered a total area of ~1 km² (Figure 6). A channel contouring a
264 small island was masked in the prediction map. Most of vegetation area was classified as seagrass by the
265 model, including patches with discolored leaves. Only a few pixels were classified as green algae (F1 score
266 of 0.55). Patches of Rhodophyceae were correctly classified (F1 score of 0.85). In the northern part of the
267 site and near the land eadges, patches of the schorre angiosperm *Sporobolus maritimus* (syn. *Spartina*
268 *maritima*) were misclassified, either as seagrass or as brown algae (F1 score of 0.77 and 0.71, respectively).

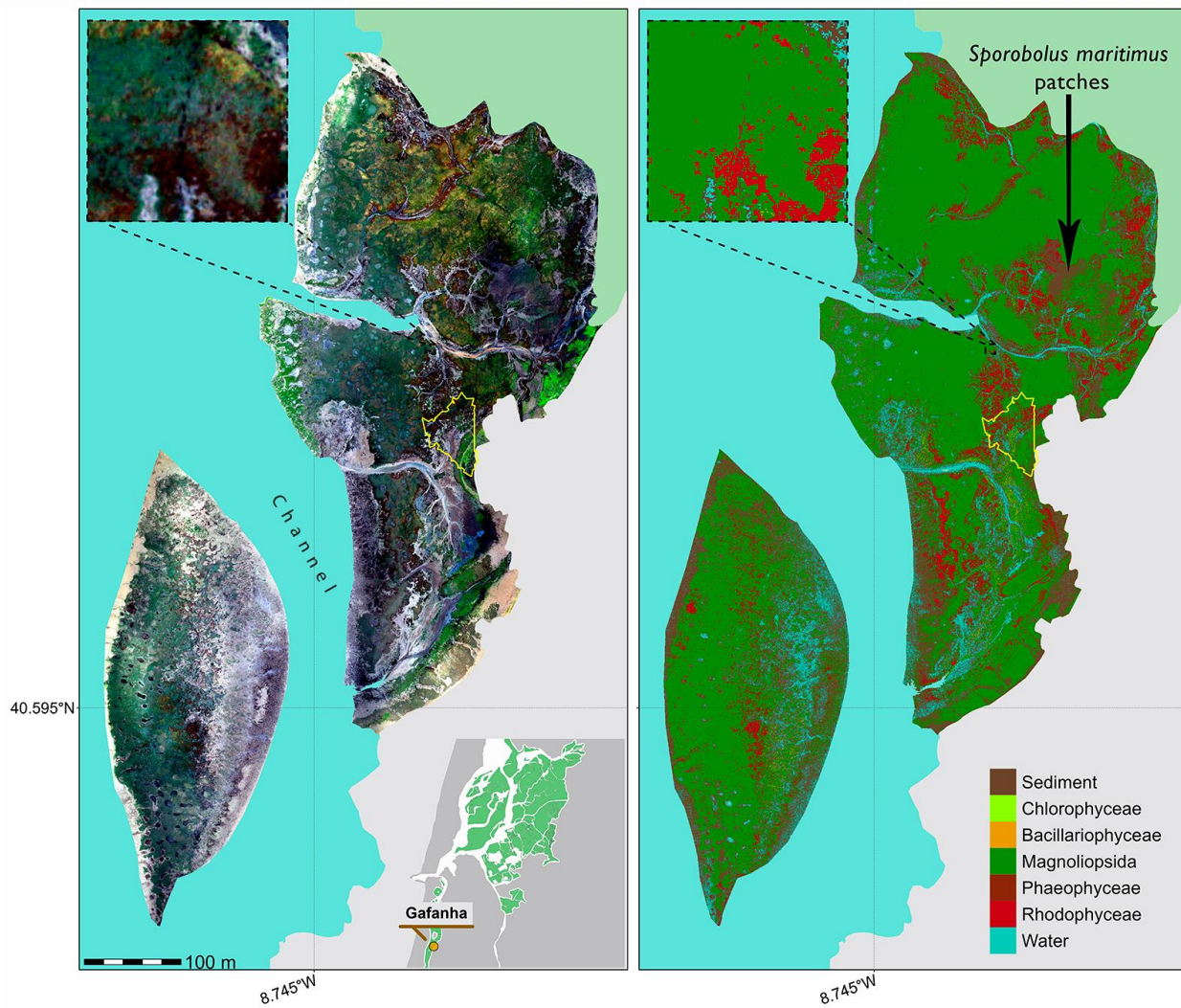


Figure 6: RGB orthomosaic (Left) and Prediction (Right) of the high-altitude flight of Gafanha, Portugal. The total extent of this flight was about 1 km² with a resolution of 80 mm per pixel. Background colors indicate intertidal area (Light Green), land area (Light Grey) and water (Light Blue). The yellow outline shows the extent of the low altitude flight of Gafanha presented in Figure 5. The zoom covers an area equivalent to a 10-meter Sentinel-2 pixel size.

269 Among the high altitude flights, the one acquired over the inner part of Ria de Aveiro coastal lagoon covered
 270 the largest area with approximately 1.5 km² (Figure 7). The vegetation present at the site was dominated by

seagrass and red macroalgae. The classification provided consistent results, with a patchy seagrass meadow mixed with red macroalgae on the eastern part of the site. As shown in the zoom (Figure 7), the edges of the meadow were mixed with green macroalgae (*Ulva sp.*), which the model agreed with (F1 score of 0.89 for green algae, 0.97 for seagrass and 0.98 for red algae).

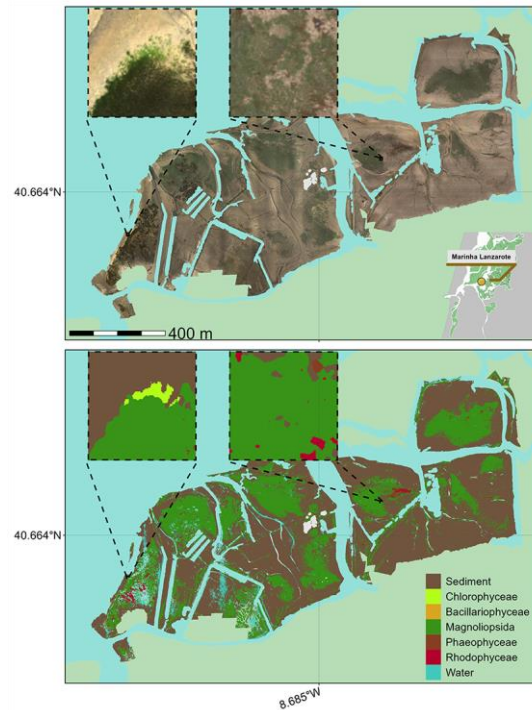


Figure 7: RGB orthomosaic (Top) and Prediction (Bottom) of the flight made in the inner part of Ria de Aveiro Lagoon, Portugal. The total extent of this flight was about 1.5 km² with a resolution of 80 mm per pixel. Background colors indicate intertidal area (Light Green), land area (Light Grey) and water (Light Blue). The zoom inserts cover an area equivalent to the size of a 10-meter Sentinel-2 pixel.

The flight over L'Epine in Noirmoutier Island, France (Figure 8 A) was conducted near a dike, which crossed the northern part of the site from West to East. Alongside this dike, Fucal brown macroalgae (*Fucus spp.*, *Ascophyllum nodosum*) were attached to sparse rocks, and stranded green algae (*Ulva spp.*)

278 could be observed, which was correctly reproduced by the prediction (Figure 8 B). This site was
279 characterized by a high mixture between green macroalgae and seagrass but these two classes were correctly
280 discriminated by the classifier (F1 score of 0.97 and 0.98 respectively).

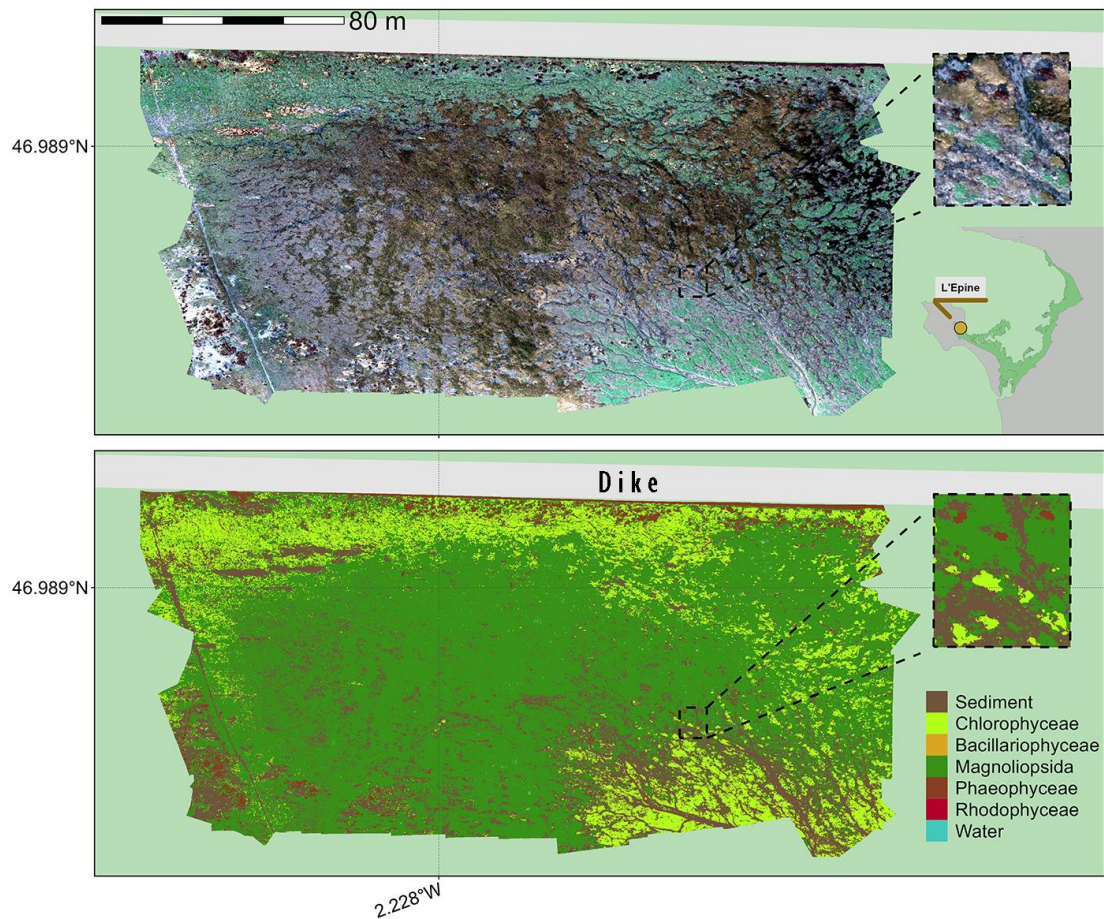


Figure 8: RGB orthomosaic (Top) and Prediction (Bottom) of L'Epine, France. The total extent of this flight was about 28 000 m² with a resolution of 80 mm per pixel. Background colors indicate intertidal area (Light Green) and land area (Light Grey). The zoom covers an area equivalent to a 10-meter Sentinel-2 pixel size.

281 **3.3 Validation of the model**

282 With all drone flights combined, the model global accuracy was 94.26% with a Kappa coefficient of 0.92
283 (Figure 9).

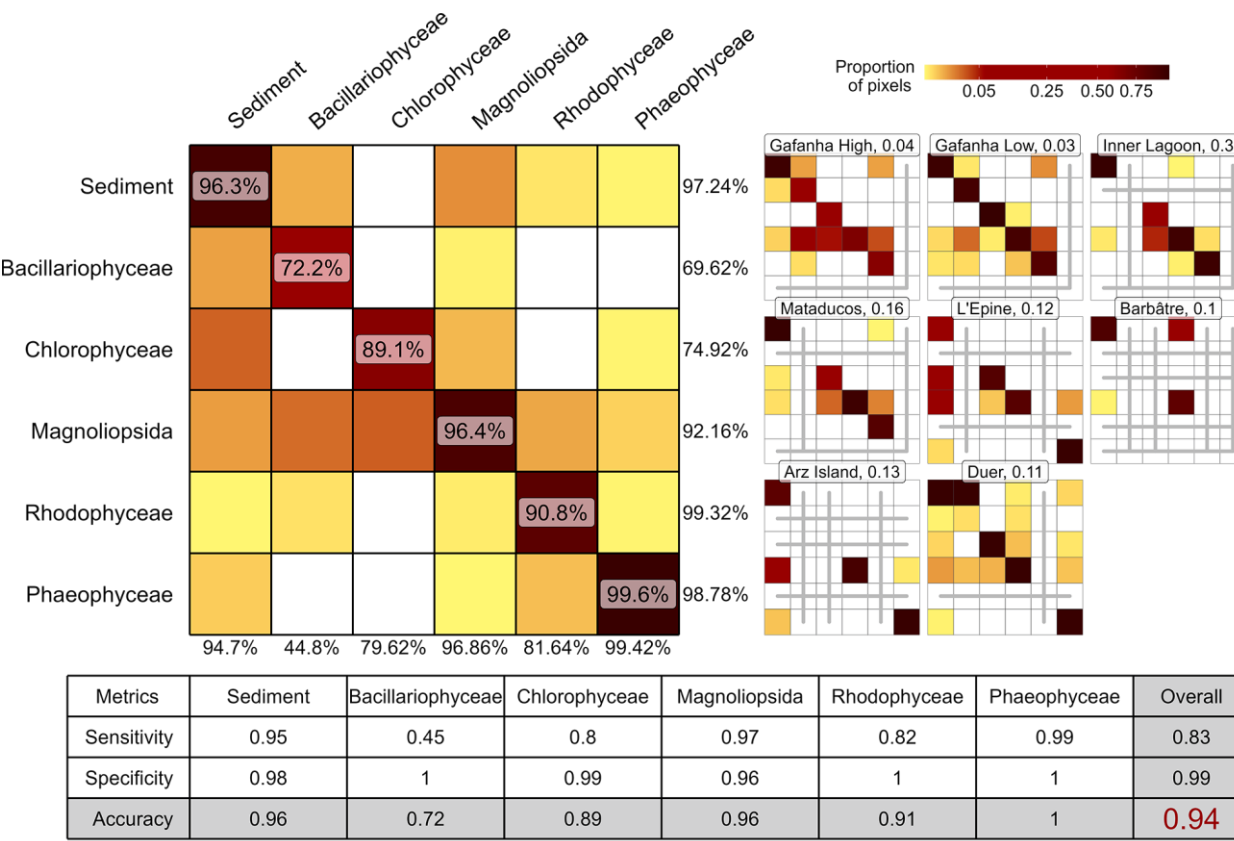


Figure 9: A global confusion matrix on the left is derived from validation data across each flight, while a mosaic of confusion matrices from individual flights is presented on the right. The labels inside the matrices indicate the balanced accuracy for each class. The labels at the bottom of the global matrix indicate the User's accuracy for each class, and those on the right indicate the Producer's Accuracy. The values adjacent to the names of each site represent the proportion of total pixels from that site contributing to the overall matrix. Grey lines within the mosaic indicate the absence of validation data for the class at that site. The table at the

bottom summarizes the Sensitivity, Specificity, and Accuracy for each class and for the overall model.

The lowest performing site was Gafanha High (global accuracy of 75.45%) whereas Mataducos was the site with the most accurate prediction (global accuracy of 98.05%). Overall, the classes Phaeophyceae, Magnoliopsida, Sediment and Rhodophyceae were correctly classified with a balanced accuracy of 1, 0.96, 0.96 and 0.91 respectively. Bacillariophyceae was the least accurate class (accuracy of 0.72) mainly due to confusion with Magnoliopsida and Sediment.

3.4 Variable importance

The computation of variable importance made it possible to identify which bands were the most useful for class prediction (Figure 10).

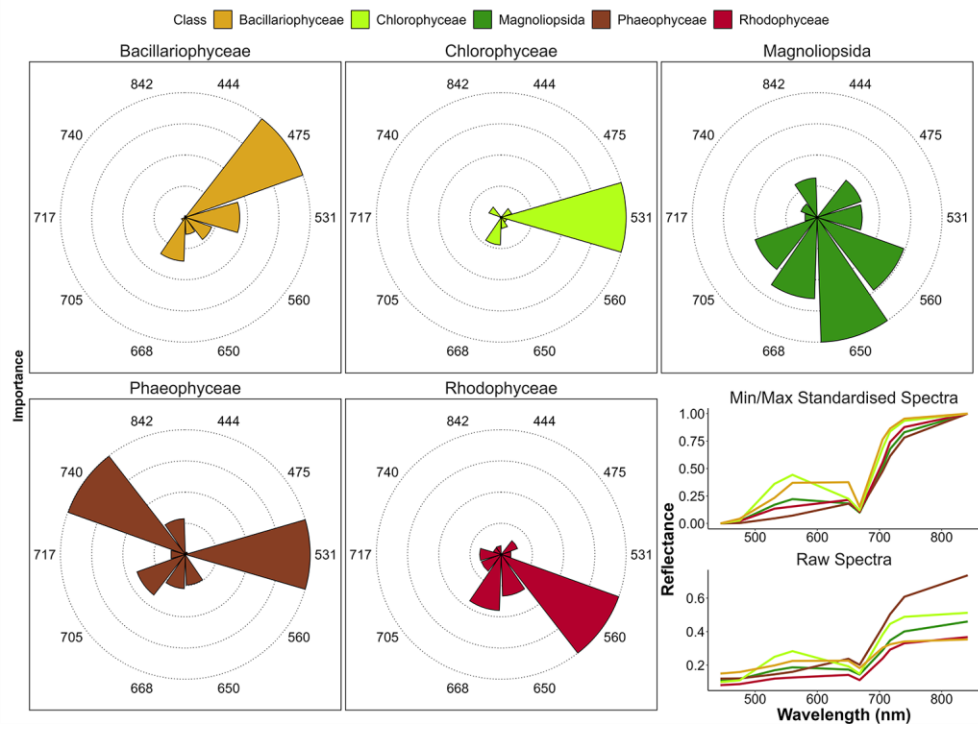


Figure 10: Variable Importance of the Neural Network Classifier for each taxonomic class.

The longer the slice, the more important the variable for prediction of each class. The right plot shows the drone raw and standardised reflectance spectra of each class. Each slice represents the Variable Importance (VI) of both raw and standardised reflectance combined.

The spectral bands at 444, 717 and 842 nm of the Micasense camera did not provide important information to discriminate any of the vegetation classes. The band at 531 nm was the most important predictor by far for the classifier to accurately predict Chlorophyceae. In fact, at this wavelength, the Chlorophyceae spectra showed the highest reflectance among all vegetation classes (Figure 2 F). The bands at 531 and 740 nm were the most important predictors for Phaeophyceae, corresponding to the lowest reflectance among all classes. Bands at 475 and 560 nm were the most important predictors for Bacillariophyceae and Rhodophyceae, respectively. Four predictors, ranging from the green (560 nm) to the RedEdge (705 nm) bands were important to accurately predict Magnoliopsida.

3.5 Effect of spatial resolution on the classification

Clear differences were seen in vegetation loss across different resolutions and vegetation classes (Figure 11). At a fine resolution of 1m, changes in the retrieved area for each vegetation type are minimal. Green algae show the highest loss, with 1.2% area lost compared to the native resolution (80 mm). As the resolution coarsens to 10m, vegetation loss becomes more pronounced, with green algae again experiencing the greatest reduction (12% compared to 8cm) and seagrass showing the smallest loss (1.3%). At a resolution of 30m, all green algae have been lost (100% compared to 8cm), while seagrass experiences a relatively small reduction of 11%. Brown algae and red algae show moderate declines, with losses at 30m resolution reaching approximately 37% and 59%, respectively.

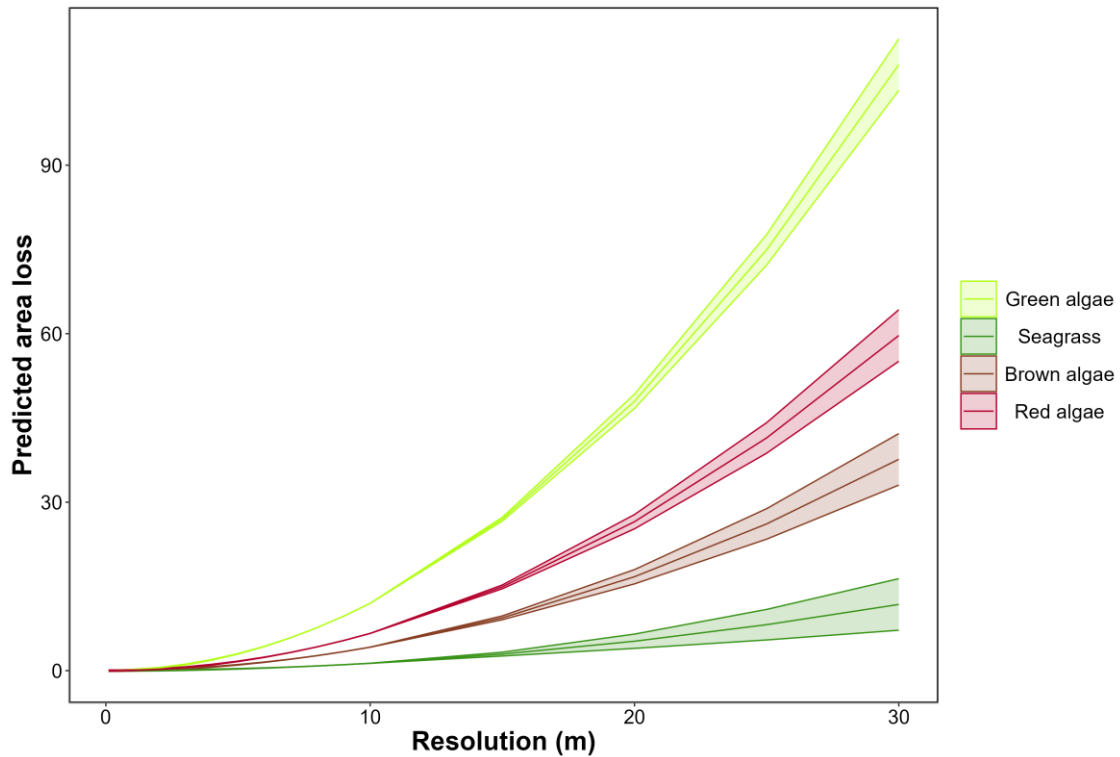


Figure 11: Predicted area loss for different vegetation types (green algae, seagrass, brown algae, red algae) as a function of spatial resolution. Lines represent GLM predictions, and shaded areas indicate standard errors. As resolution decreases, predicted area loss increases for all vegetation types, with green algae showing the highest loss and seagrass the smallest at coarser resolutions.

3.6 Effect of the percent cover on the prediction

Using the very high resolution low altitude flight (8 mm pixels), we determined the minimal percent cover required to correctly classify a given class within the corresponding high altitude flight (8cm pixel resolution ; [Figure 12](#)).

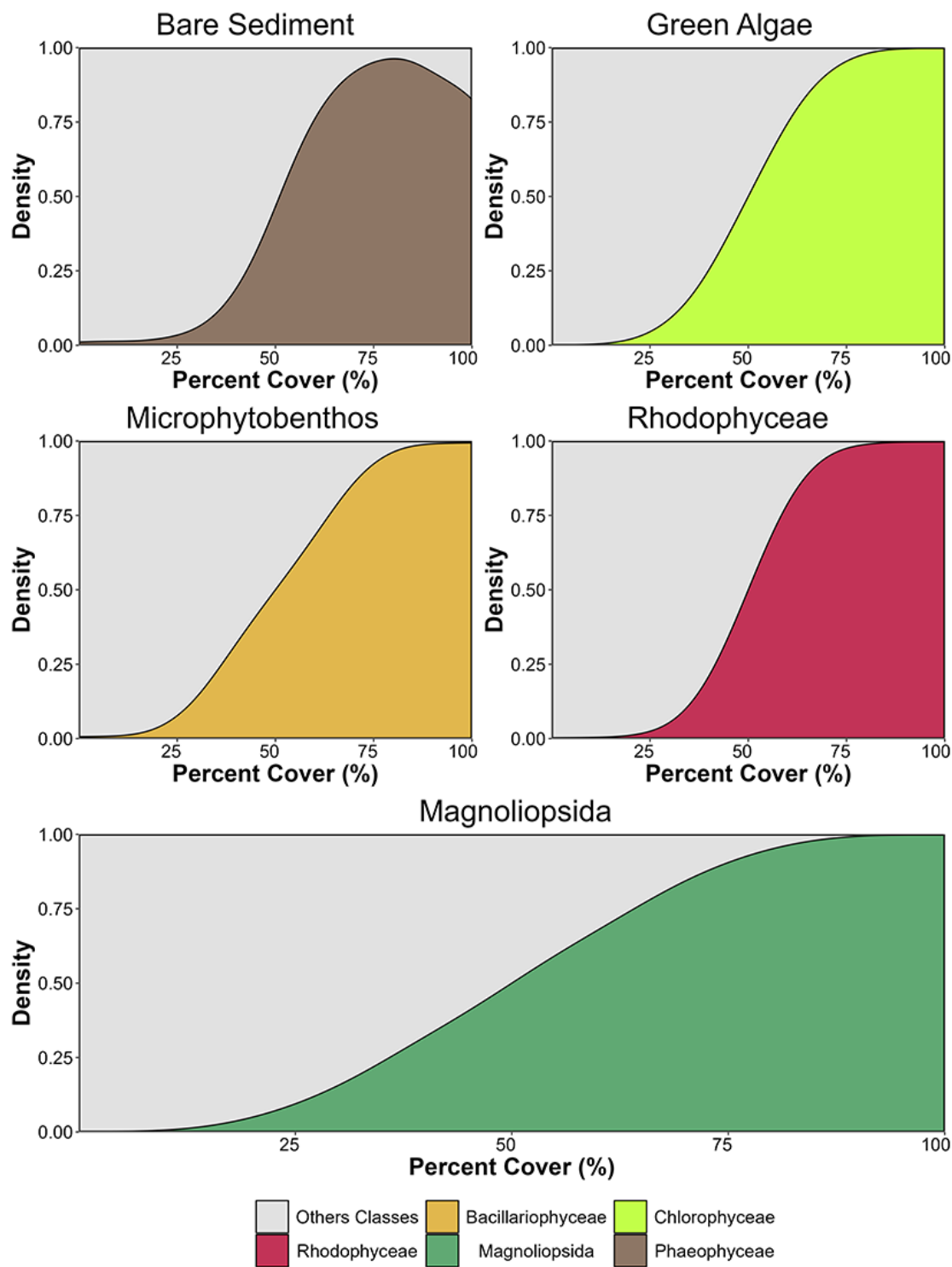


Figure 12: Kernel density plot showing the proportion of pixel well classified based on the percent cover of the class in high altitude flight pixels of Gafanha, Portugal. Each subplot

shows all the pixels of the same classes on the high altitude flight. Percent cover of classes was retrieved using the result of the classification of the low altitude flight of Gafanha, Portugal.

A percent cover of at least 80% was sufficient to have all the 80 mm pixels correctly classified, with the exception of Magnoliopsida that required a higher cover (>90 %) to be accurately classified. Concerning the probability of each class, there is a linear relationship between the percent cover and the confidence of the model to predict the class. To predict Chlorophyceae with a model likelihood of 0.85, a cover of 93 % was needed, 90 % for Magnoliopsida, 92 % for Rhodophyceae and 97 % for Bacillariophyceae. When the vegetation cover of a given class was 100 %, coarser high-flight pixels were correctly classified for all the classes except for Bare Sediment, which was only correctly classified 80% of the time. This phenomenon may be attributed to the time gap between the two flights, allowing for microphytobenthos migration to the surface during low tide, consequently altering the model's classification from bare sediment to Bacillariophyceae.

4. Discussion

4.1 Vegetation Discrimination

The primary objective of this study was to develop a method for the accurate classification of emerged macrophytes observed during low tide on tidal flats, specifically focusing on distinguishing between Chlorophyceae (green macroalgae) and marine Magnoliopsida (seagrasses) using a multispectral resolution. The discrimination between seagrasses and green macroalgae is challenging due to their optical similarity in the visible range (Bannari et al., 2022; Oiry and Barillé, 2021; Veetil et al., 2020). These two macrophytes share a similar pigment composition: chlorophyll-a (common to all vegetation types), chlorophyll-b (an additional photosynthetic pigment), and accessory carotenoids such as zeaxanthin, lutein

and neoxanthin (Figure 13). Their spectral responses could be close, particularly at a multispectral resolution. Seagrass and green macroalgae frequently co-occur in intertidal areas and can intermingle within a remote sensing pixel if the spatial resolution is too low. Here, the issue of intra-pixel mixing was resolved thanks to the very high spatial resolution of the drone (from 8 to 80 mm). In this study the risk of spectral confusion was avoided with a machine-learning approach exploiting a neural networks classifier. Our drone flights and a recent study based on *in situ* radiometry, suggested that a sensor with at least eight spectral bands ranging from 500 to 850 nm, and including a green band at 530 nm and a RedEdge band at 730 nm, was crucial to accurately discriminate green macroalgae from seagrasses (Davies et al., 2023a).

	Chl-b	Chl-c	Fuco	Zea	Diad	Lut	Neo	PE	PC
Magnoliopsida	Green	Red	Red	Green	Red	Green	Green	Red	Red
Chlorophyceae	Green	Red	Red	Green	Red	Green	Green	Red	Red
Bacillariophy.	Red	Green	Green	Red	Green	Red	Red	Red	Red
Phaeophyceae	Red	Green	Green	Green	Red	Red	Red	Red	Red
Rhodophyceae	Red	Red	Red	Red	Red	Red	Red	Green	Green
Absorption (nm)	650	636	550	489	496	490	450	566	615

Figure 13: Photosynthetic and carotenoid pigments present (Green) or absent (Red) in each taxonomic class present in the Neural Network Classifier, along with their absorption wavelength measured with spectroradiometer, Chl-b: chlorophyll-b, Chl-c: chlorophyll-c, Fuco: fucoxanthin, Zea: zeaxanthin, Diad: diadinoxanthin, Lut: lutein, Neo: neoxanthin, PE: phycoerythrin, PC: phycocyanin Christensen et al. (1977).

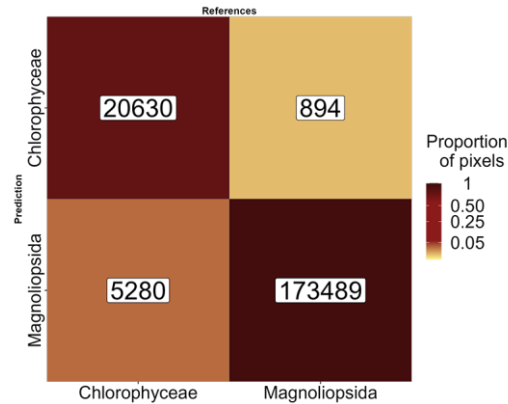


Figure 14: Sample of Figure 9 focusing on green macrophytes. The labels inside the matrix indicate the number of pixels.

Meeting these two criteria, the Micasense RedEdge-MX DUAL camera used in this study, enabled the classifier to achieve 97% of accuracy between these two classes (Figure 14). Even if their pigment composition is similar, differences in the spectral shape can be observed, with green algae having a higher reflectance peak at 560 nm as well as a higher NIR plateau than seagrass (Figure 2). Such differences were previously attributed to differences in pigments concentration and/or ratios (Bargain et al., 2013), cellular structure as well as in the orientation of the plant at the sediment surface (Beach et al., 1997; Hedley et al., 2018; Kirk, 1994).

The variable importance analysis (Figure 10) identified that the band at 531 nm was the most important for accurately identifying Chlorophyceae. In fact, at this wavelength, Chlorophyceae exhibited the highest reflectance among all other classes, highlighting the difference in carotenoid to chlorophyll-a ratios between seagrasses and green macroalgae (Repolho et al., 2017). Concerning Phaeophyceae, the thick cell walls of these macroalgae (Charrier et al., 2021) make it more reflective in the infrared part of the spectra (Slaton et al., 2001), while the presence of fucoxanthin and zeaxanthin result in a low reflectance in the visible region (Figure 10 ; Figure 13). These two key features have been identified by the Neural Network as the two principal predictors to accurately identify brown algae (Figure 10). Similarly, the presence of phycoerythrin

and phycocyanin in Rhodophyceae contributes to the lowest reflectance among all classes in the spectral range from 560 to 615 nm (Figure 10). Indeed, the band at 560 nm has been identified as important for identifying this class, likely due to phycoerythrin absorption at this wavelength. Regarding Bacillariophyceae, 475 nm was the most important predictor for this class (Figure 10). Indeed, the reflectance at 475 nm was higher for Bacillariophyceae than for any other vegetation class (Figure 2), very likely due to the low biomass (and associated concentration of blue-absorbing pigments) of these unicellular organisms compared to seagrass and macroalgae.

4.2 Altitude and Temporal Effects on Vegetation Prediction Accuracy

The ability to differentiate between various types of vegetation plays a critical role in ecological monitoring and coastal management (European-Commission, 2000). By distinguishing between seagrasses and macroalgae, our approach facilitates targeted conservation strategies, enabling more effective preservation and restoration efforts in coastal ecosystems. While comparing the reflectance at two different altitudes (12 m and 120 m with a spatial resolution of 8 and 80 mm, respectively), a nearly one-to-one relationship was observed, with a Root Mean Square Error (RMSE) of 0.02 (Figure 4). This result indicates that the reflectance measured by remote sensing (RS) sensors is not significantly influenced by pixel size. This finding is valuable for integrating drone-based data into larger-scale mapping projects (e.g., combining satellite and drone mapping in side-by-side analyses). The consistency of reflectance across altitudes suggests that drones can be effectively used for finer-scale mapping without compromising data accuracy when merging with other platforms. However, it was observed that there is an underestimation of the infrared part of the spectra in the high-altitude dataset (Figure 4). Such disparity in infrared reflectance may stem from temporal differences between the flights, possibly resulting in a slightly drier intertidal area and consequently higher infrared reflectance. This disparity poses an issue for the methodology followed in the present study, relying solely on one flight height for training. To address this issue, we employed min/max standardized reflectance spectra as predictors for the model Equation 1. This approach allowed us to

eliminate the slight reflectance difference between the flights (Figure 4 B) and to focus on the shape of the spectra in the visible part of the electromagnetic spectra, where different pigmentation are associated to taxonomic diagnostic features. In contrast to subtidal seagrasses, which maintain a relatively constant biomass throughout the year, intertidal seagrasses, like the one studied in this work, exhibit strong seasonal phenology (Davies et al., 2024b). At some sites, they completely disappear during the winter and reach their peak above-ground biomass in the summer and early autumn. Along with these seasonal changes in biomass, the pigment composition and ratios also vary throughout the year, reflecting the plants' adaptations to different environmental conditions (Bargain et al., 2013; Légaré et al., 2022). Standardization of spectral signatures helps to mitigate the impact of changing biomass on the spectral profile, enabling the development of a model that can reliably predict vegetation across different geographical locations and seasons. This approach allows for consistent classification of vegetation despite variations in biomass and fluctuations in light conditions, providing a robust tool for monitoring and predicting vegetation dynamics (Costa et al., 2021; Fyfe, 2003; Piasek et al., 2023). We found 90 % seagrass cover was necessary at an 8 cm resolution for confident prediction of its presence (Figure 12). However, due to the strong phenology of intertidal seagrass meadows in Europe, the period when a meadow is well-established can be temporally restricted, limiting the ideal window for accurate detection.

4.3 Impact of Pixel Resolution on the prediction and Implications for Satellite Remote Sensing

Pixel resolution plays a critical role in accurately retrieving vegetation area from remote sensing data. As pixel size increases, we found a consistent decline in area retrieval is observed across all vegetation types, with more pronounced effects for certain types, such as green algae (Figure 11). This highlights the sensitivity of spatial resolution in detecting smaller or more fragmented vegetation features. Green algae, being particularly patchy across all study sites, shows the steepest decline in areal agreement as pixel size

increases, which aligns with expectations given the limitations of coarser resolution in capturing fine-scale details.

This resolution-area relationship has important implications for satellite missions like Sentinel-2 and Landsat, which are commonly used in marine and coastal vegetation studies. Both satellites offer high-resolution imagery, with pixel sizes of 10m and 30m, respectively. While these resolutions are suitable for broad-scale environmental monitoring, they may be too coarse to capture finer-scale heterogeneity, particularly in fragmented vegetation like green algae. Our findings suggest that, while the 30m resolution of Landsat may be adequate for homogeneous vegetation types, such as seagrass, a higher resolution is essential for accurately mapping patchy vegetation like green algae. These findings have direct implications for environmental management and conservation planning. Overlooking fine-scale vegetation features, such as those seen in green algae, could result in inadequate protection or restoration efforts, particularly in ecologically sensitive coastal zones, as early stages of green tides could be challenging to monitor at coarse resolutions.

Very high-resolution imagery offers more accurate vegetation mapping but comes with trade-offs. As resolution increases, data costs rise, and processing becomes more resource-intensive due to the larger file sizes and computational demands. Consequently, high-resolution data requires more storage and can slow down real-time applications. For large-scale monitoring of homogeneous vegetation types, 10 m resolution of S2/MSI or even the 30 m of Landsat/OLI are often sufficient. However, when mapping fragmented vegetation like green algae, the precision provided by higher-resolution imagery is crucial, despite the additional costs and processing challenges it imposes.

4.4 Towards climate and biodiversity applications

Climate change, global warming, eutrophication, alien and invasive species development, coastal erosion, and sea level rise are expected to continue impacting coastal ecosystems in the future (Holon et al., 2018; Marquet et al., 2024; Schibalski et al., 2022) and the demand for meaningful and efficient monitoring of

coastal habitats has never been higher (Muller-Karger et al., 2018; Oiry and Barillé, 2021; Villalobos Perna et al., 2023). Our findings, particularly the improved discrimination of intertidal seagrass and green macroalgae from other intertidal vegetation classes, highlight the potential of drone-based remote sensing to support diverse applications, from conservation of biodiversity to climate change adaptation strategies.

Due to increasing coastal eutrophication, macroalgal blooms are becoming increasingly common in many regions around the world (Sutton et al., 2011; Ye et al., 2011). These blooms can have negative impacts on human health and local economic activities, including human health, fishing and aquaculture, tourism, and recreational activities (Villares et al., 1999; Ye et al., 2011). The first green tide events (i.e. bloom of green macroalgae of the genus *Ulva*) were reported in Brittany, France, in the 1970s and have since been a concern for local stakeholders and economic activities (Ménèsguen, 2018). Some regions of the world have witnessed an increase in brown macroalgae blooms, predominantly involving algae of the genus *Sargassum* washing along the Caribbean coastlines (Louime et al., 2017), and more recently *Rugulopteryx okamurea* in southern Europe (Roca et al., 2022). Satellite remote sensing has proven to be a valuable tool for mapping the spatial and temporal extent of macroalgal blooms worldwide. However, due to limitations in spatial resolution, it can only effectively map well-developed blooms (Haro et al., 2023; Klemas, 2012; Schreyers et al., 2021). High spatial resolution drone imagery, coupled with accurate classification algorithm, could be used to map the early stages of macroalgal blooms in areas known to have regular blooms or in new sites. Indeed, this approach could provide early warning alerts to local managers and complementary to traditional sampling methods to monitor coastal ecosystems. These methods are generally time and resource-intensive, and the findings are often difficult to scale-up when applied alone. Earth Observation can bridge this gap and meet the needs for systematic monitoring of coastal ecosystems over large areas (Papathanasopoulou et al., 2019). The retrieval of Essential Biodiversity Variables and Essential Ocean Variables through satellite observations has been increasingly common, enabling comprehensive monitoring of entire ecosystems over extended time periods (Ratnarajah et al., 2023; Zoffoli et al., 2021). The Water Framework Directive (European-Commission, 2000) mandates the achievement and

451 maintenance of “good ecological status” for all European waters, which necessitates a comprehensive
452 understanding and monitoring of aquatic ecosystems, including coastal habitats like seagrass beds (Foden
453 and Brazier, 2007; Nordlund et al., 2024; Zoffoli et al., 2021).

454 Effective and efficient monitoring tools are essential for identifying the impacts of human activities and
455 natural changes on coastal ecosystems. On-demand, multispectral drone observations at very high spatial-
456 resolution provide a novel and powerful tool to rapidly and accurately acquire ground truth data which can
457 be used to develop machine-learning algorithm for satellite sensors (Davies et al., 2024a). Spatially resolved
458 data are indeed critical for calibrating and validating satellite remote sensing observations, thereby
459 enhancing our capacity to monitor vast coastal areas. The integration of drone technology facilitates a
460 scalable approach to environmental surveillance while taking into account patchiness of secondary
461 vegetation, offering significant advancements in the spatial and temporal resolution of data collection. This,
462 in turn, supports the EU WFD’s objectives by enabling more informed and timely management decisions
463 for the conservation and restoration of aquatic ecosystems.

464 **5. Conclusion**

465 The utilization of very high spatial resolution (from 8 to 80 mm) drone-based remote sensing coupled with
466 machine learning techniques has proven to be an effective method for the discrimination of intertidal
467 seagrasses from green macroalgae with a multispectral resolution sensor. Standardized reflectance was
468 incorporated in the Neural Network model allowing for better discrimination of spectral features related to
469 pigment absorption in the visible region of the spectrum. There was a striking difference between the
470 variable of importance to discriminate Magnoliopsida from Chlorophyceae. The latter was essentially
471 identified with the 451 nm spectral band while more spectral bands were needed to identify the former,
472 notably 650, 560, 668, and 705 nm. As the spectral bands of the Micasense RedEdge Dual MX are very
473 similar to those of Sentinel-2/MSI, we suggest that multispectral satellite data have the potential to perform

474 this discrimination between these green macrophytes. The findings underscore the importance of adopting
475 advanced remote sensing tools in ecological studies and environmental monitoring, providing a foundation
476 for future research and policy implementation aimed at ecosystem conservation and restoration.

477 Adade, R., Aibinu, A.M., Ekumah, B., Asaana, J., 2021. Unmanned aerial vehicle (UAV) applications in
478 coastal zone management—a review. *Environmental Monitoring and Assessment* 193, 1–12.

479 Agisoft, 2019. [Agisoft metashape](#).

480 Angnuureng, D.B., Brempong, K., Jayson-Quashigah, P., Dada, O., Akuoko, S., Frimpomaa, J., Mattah, P.,
481 Almar, R., 2022. Satellite, drone and video camera multi-platform monitoring of coastal erosion at an
482 engineered pocket beach: A showcase for coastal management at elmina bay, ghana (west africa). *Regional*
483 *Studies in Marine Science* 53, 102437.

484 Bannari, A., Ali, T.S., Abahussain, A., 2022. The capabilities of sentinel-MSI (2A/2B) and landsat-OLI
485 (8/9) in seagrass and algae species differentiation using spectral reflectance. *Ocean Science* 18, 361–388.

486 Bargain, A., Robin, M., Méléder, V., Rosa, P., Le Menn, E., Harin, N., Barillé, L., 2013. Seasonal spectral
487 variation of *zostera noltii* and its influence on pigment-based vegetation indices. *Journal of experimental*
488 *marine biology and ecology* 446, 86–94.

489 Beach, K., Borgeas, H., Nishimura, N., Smith, C., 1997. In vivo absorbance spectra and the ecophysiology
490 of reef macroalgae. *Coral Reefs* 16, 21–28.

491 Brunier, G., Oiry, S., Gruet, Y., Dubois, S.F., Barillé, L., 2022. Topographic analysis of intertidal
492 polychaete reefs (*sabellaria alveolata*) at a very high spatial resolution. *Remote Sensing* 2022, Vol. 14, Page
493 307 14, 307. <https://doi.org/10.3390/RS14020307>

494 Cao, J., Thorson, J.T., Richards, R.A., Chen, Y., 2017. Spatiotemporal index standardization improves the
495 stock assessment of northern shrimp in the gulf of maine. *Canadian Journal of Fisheries and Aquatic*
496 *Sciences* 74, 1781–1793. <https://doi.org/10.1139/cjfas-2016-0137>

497 Cartaxana, P., Cruz, S., Gameiro, C., Kühl, M., 2016. Regulation of intertidal microphytobenthos
 498 photosynthesis over a diel emersion period is strongly affected by diatom migration patterns. *Frontiers in*
 499 *microbiology* 7, 872.

500 Casella, E., Drechsel, J., Winter, C., Benninghoff, M., Rovere, A., 2020. Accuracy of sand beach
 501 topography surveying by drones and photogrammetry. *Geo-Marine Letters* 40, 255–268.

502 Charrier, B., Boscq, S., Nelson, B.J., Läubli, N.F., 2021. Growth and labelling of cell wall components of
 503 the brown alga *ectocarpus* in microfluidic chips. *Frontiers in Marine Science* 8, 745654.

504 Chefaoui, R.M., Duarte, C.M., Serrão, E.A., 2018. Dramatic loss of seagrass habitat under projected climate
 505 change in the mediterranean sea. *Global change biology* 24, 4919–4928.

506 Christensen, T., Dixon, P.S., Irvine, L.M., 1977. Seaweeds of the british isles: Tribophyceae
 507 (xanthophyceae). British Museum (Natural History).

508 Coffey, M.M., Graybill, D.D., Whitman, P.J., Schaeffer, B.A., Salls, W.B., Zimmerman, R.C., Hill, V.,
 509 Lebrasse, M.C., Li, J., Keith, D.J., others, 2023. Providing a framework for seagrass mapping in united
 510 states coastal ecosystems using high spatial resolution satellite imagery. *Journal of Environmental*
 511 *Management* 337, 117669.

512 Collin, A., Dubois, S., James, D., Houet, T., 2019. Improving intertidal reef mapping using UAV surface,
 513 red edge, and near-infrared data. *Drones* 3, 67.

514 Costa, V., Serôdio, J., Lillebø, A.I., Sousa, A.I., 2021. Use of hyperspectral reflectance to non-destructively
 515 estimate seagrass *zostera noltei* biomass. *Ecological Indicators* 121, 107018.
 516 [https://doi.org/https://doi.org/10.1016/j.ecolind.2020.107018](https://doi.org/10.1016/j.ecolind.2020.107018)

517 Davies, B.F.R., Gernez, P., Geraud, A., Oiry, Simon, Rosa, P., Zoffoli, M.L., Barillé, L., 2023a. Multi- and
 518 hyperspectral classification of soft-bottom intertidal vegetation using a spectral library for coastal

519 biodiversity remote sensing. Remote Sensing of Environment 290, 113554.
520 <https://doi.org/10.1016/j.rse.2023.113554>

521 Davies, B.F.R., Oiry, S., Rosa, P., Zoffoli, M.L., Sousa, A.I., Thomas, O.R., Smale, D.A., Austen, M.C.,
522 Biermann, L., Attrill, M.J., others, 2024b. A sentinel watching over inter-tidal seagrass phenology across
523 western europe and north africa. Communications Earth & Environment 5, 382.

524 Davies, B.F.R., Oiry, S., Rosa, P., Zoffoli, M.L., Sousa, A.I., Thomas, O.R., Smale, D.A., Austen, M.C.,
525 Biermann, L., Attrill, M.J., others, 2024a. Intertidal seagrass extent from sentinel-2 time-series show
526 distinct trajectories in western europe. Remote Sensing of Environment 312, 114340.

527 Davies, B.F.R., Sousa, A.I., Figueira, R., Oiry, S., Gernez, P., Barillé, L., 2023b. Benthic intertidal
528 vegetation from the tagus estuary and aveiro lagoon. <https://doi.org/10.15468/n4ak6x>

529 Devlin, M., Brodie, J., 2023. Nutrients and eutrophication, in: Marine Pollution–Monitoring, Management
530 and Mitigation. Springer, pp. 75–100.

531 Douay, F., Verpoorter, C., Duong, G., Spilmont, N., Gevaert, F., 2022. New hyperspectral procedure to
532 discriminate intertidal macroalgae. Remote Sensing 14. <https://doi.org/10.3390/rs14020346>

533 Duffy, J.E., Benedetti-Cecchi, L., Trinanes, J., Muller-Karger, F.E., Ambo-Rappe, R., Boström, C.,
534 Buschmann, A.H., Byrnes, J., Coles, R.G., Creed, J., others, 2019. Toward a coordinated global observing
535 system for seagrasses and marine macroalgae. Frontiers in Marine Science 6, 317.

536 European-Commission, 2000. “DIRECTIVE 2000/60/EC OF THE EUROPEAN PARLIAMENT AND OF
537 THE COUNCIL of 23 October 2000 establishing a framework for Community action in the field of water
538 policy” or, in short, the EU Water Framework Directive. Official Journal of the European Communities L
539 327, 1–72.

540 Fairley, I., Williamson, B.J., McIlvenny, J., King, N., Masters, I., Lewis, M., Neill, S., Glasby, D., Coles,
541 D., Powell, B., others, 2022. Drone-based large-scale particle image velocimetry applied to tidal stream
542 energy resource assessment. *Renewable Energy* 196, 839–855.

543 Foden, J., Brazier, D., 2007. Angiosperms (seagrass) within the EU water framework directive: A UK
544 perspective. *Marine Pollution Bulletin* 55, 181–195.

545 Fyfe, S., 2003. Spatial and temporal variation in spectral reflectance: Are seagrass species spectrally
546 distinct? *Limnology and Oceanography* 48, 464–479.

547 Gardner, R.C., Finlayson, C., 2018. Global wetland outlook: State of the world’s wetlands and their services
548 to people. *Stetson Law*.

549 Haro, S., Jimenez-Reina, J., Bermejo, R., Morrison, L., 2023. BioIntertidal mapper software: A satellite
550 approach for NDVI-based intertidal habitat mapping. *SoftwareX* 24, 101520.

551 Hedley, J.D., Mirhakak, M., Wentworth, A., Dierssen, H.M., 2018. Influence of three-dimensional coral
552 structures on hyperspectral benthic reflectance and water-leaving reflectance. *Applied Sciences* 8, 2688.

553 Holon, F., Marre, G., Parravicini, V., Mouquet, N., Bockel, T., Descamp, P., Tribot, A.-S., Boissery, P.,
554 Deter, J., 2018. A predictive model based on multiple coastal anthropogenic pressures explains the
555 degradation status of a marine ecosystem: Implications for management and conservation. *Biological*
556 *Conservation* 222, 125–135.

557 Howard, J., others, 2018. *Fastai*.

558 Jankowska, E., Michel, L.N., Lepoint, G., Włodarska-Kowalczyk, M., 2019. Stabilizing effects of seagrass
559 meadows on coastal water benthic food webs. *Journal of Experimental Marine Biology and Ecology* 510,
560 54–63.

561 Joyce, K.E., Fickas, K.C., Kalamandeen, M., 2023. The unique value proposition for using drones to map
562 coastal ecosystems. *Cambridge Prisms: Coastal Futures* 1, e6.

563 Kirk, J.T., 1994. *Light and photosynthesis in aquatic ecosystems*. Cambridge university press.

564 Klemas, V., 2012. Remote sensing of algal blooms: An overview with case studies. *Journal of coastal*
565 *research* 28, 34–43.

566 Légaré, B., Bélanger, S., Singh, R.K., Bernatchez, P., Cusson, M., 2022. Remote sensing of coastal
567 vegetation phenology in a cold temperate intertidal system: Implications for classification of coastal
568 habitats. *Remote Sensing* 14, 3000.

569 Lin, H., Sun, T., Zhou, Y., Gu, R., Zhang, X., Yang, W., 2018. Which genes in a typical intertidal seagrass
570 (*zostera japonica*) indicate copper-, lead-, and cadmium pollution? *Frontiers in Plant Science* 9, 1545.

571 Los Santos, C.B. de, Krause-Jensen, D., Alcoverro, T., Marbà, N., Duarte, C.M., Van Katwijk, M.M., Pérez,
572 M., Romero, J., Sánchez-Lizaso, J.L., Roca, G., others, 2019. Recent trend reversal for declining european
573 seagrass meadows. *Nature communications* 10, 3356.

574 Louime, C., Fortune, J., Gervais, G., 2017. Sargassum invasion of coastal environments: A growing
575 concern. *American Journal of Environmental Sciences* 13, 58–64.

576 Marquet, P.A., Buschmann, A.H., Corcoran, D., Díaz, P.A., Fuentes-Castillo, T., Garreaud, R., Pliscoff, P.,
577 Salazar, A., 2024. Global change and acceleration of anthropic pressures on patagonian ecosystems, in:
578 *Conservation in Chilean Patagonia: Assessing the State of Knowledge, Opportunities, and Challenges*.
579 Springer International Publishing Cham, pp. 33–65.

580 Méléder, V., Laviale, M., Jesus, B., Mouget, J.L., Lavaud, J., Kazemipour, F., Launeau, P., Barillé, L.,
581 2013. In vivo estimation of pigment composition and optical absorption cross-section by spectroradiometry
582 in four aquatic photosynthetic micro-organisms. *Journal of Photochemistry and Photobiology B: Biology*
583 129, 115–124.

584 Ménesguen, A., 2018. Les marées vertes: 40 clés pour comprendre. Editions Quae.

585 Miloslavich, P., Bax, N.J., Simmons, S.E., Klein, E., Appeltans, W., Aburto-Oropeza, O., Garcia, M.A.,
586 Batten, S.D., Benedetti-Cecchi, L., Checkley, D.M., Chiba, S., Duffy, J.E., Dunn, D.C., Fischer, A., Gunn,
587 J., Kudela, R., Marsac, F., Muller-Karger, F.E., Obura, D., Shin, Y.J., 2018. Essential ocean variables for
588 global sustained observations of biodiversity and ecosystem changes. *Global Change Biology* 24, 2416–
589 2433. <https://doi.org/10.1111/GCB.14108>

590 Muller-Karger, F.E., Hestir, E., Ade, C., Turpie, K., Roberts, D.A., Siegel, D., Miller, R.J., Humm, D.,
591 Izenberg, N., Keller, M., others, 2018. Satellite sensor requirements for monitoring essential biodiversity
592 variables of coastal ecosystems. *Ecological applications* 28, 749–760.

593 Nebel, S., Beege, M., Schneider, S., Rey, G.D., 2020. A review of photogrammetry and photorealistic 3D
594 models in education from a psychological perspective, in: *Frontiers in Education*. Frontiers Media SA, p.
595 144.

596 Nguyen, H.M., Ralph, P.J., Marín-Guirao, L., Pernice, M., Procaccini, G., 2021. Seagrasses in an era of
597 ocean warming: A review. *Biological Reviews* 96, 2009–2030.

598 Nijland, W., Reshitnyk, L., Rubidge, E., 2019. Satellite remote sensing of canopy-forming kelp on a
599 complex coastline: A novel procedure using the landsat image archive. *Remote Sensing of Environment*
600 220, 41–50.

601 Nordlund, L.M., Unsworth, R.K., Wallner-Hahn, S., Ratnarajah, L., Beca-Carretero, P., Boikova, E., Bull,
602 J.C., Chefaoui, R.M., Santos, C.B. de los, Gagnon, K., others, 2024. One hundred priority questions for
603 advancing seagrass conservation in europe. *Plants, People, Planet*.

604 Oh, J., Kim, D., Lee, H., 2017. Use of a drone for mapping and time series image acquisition of tidal zones.
605 *Journal of the Korean Institute of Intelligent Systems* 27, 119–125.

606 Oiry, S., Barillé, L., 2021. Using sentinel-2 satellite imagery to develop microphytobenthos-based water
607 quality indices in estuaries. *Ecological Indicators* 121, 107184.

608 Orth, R.J., Carruthers, T.J., Dennison, W.C., Duarte, C.M., Fourqurean, J.W., Heck, K.L., Hughes, A.R.,
609 Kendrick, G.A., Kenworthy, W.J., Olyarnik, S., others, 2006. A global crisis for seagrass ecosystems.
610 *Bioscience* 56, 987–996.

611 Papathanasopoulou, E., Simis, S., Alikas, K., Ansper, A., Anttila, J., Barillé, A., Barillé, L., Brando, V.,
612 Bresciani, M., Bučas, M., others, 2019. Satellite-assisted monitoring of water quality to support the
613 implementation of the water framework directive. EOMORES white paper.

614 Pereira, H.M., Ferrier, S., Walters, M., Geller, G.N., Jongman, R.H., Scholes, R.J., Bruford, M.W.,
615 Brummitt, N., Butchart, S.H., Cardoso, A., others, 2013. Essential biodiversity variables. *Science* 339, 277–
616 278.

617 Piaser, E., Berton, A., Bolpagni, R., Caccia, M., Castellani, M.B., Coppi, A., Dalla Vecchia, A.,
618 Gallivanone, F., Sona, G., Villa, P., 2023. Impact of radiometric variability on ultra-high resolution
619 hyperspectral imagery over aquatic vegetation: Preliminary results. *IEEE Journal of Selected Topics in*
620 *Applied Earth Observations and Remote Sensing*.

621 Ralph, P., Polk, S., Moore, K., Orth, R., Smith Jr, W., 2002. Operation of the xanthophyll cycle in the
622 seagrass *zostera marina* in response to variable irradiance. *Journal of Experimental Marine Biology and*
623 *Ecology* 271, 189–207.

624 Rasheed, M.A., Unsworth, R.K., 2011. Long-term climate-associated dynamics of a tropical seagrass
625 meadow: Implications for the future. *Marine Ecology Progress Series* 422, 93–103.

626 Ratnarajah, L., Abu-Alhaija, R., Atkinson, A., Batten, S., Bax, N.J., Bernard, K.S., Canonico, G., Cornils,
627 A., Everett, J.D., Grigoratou, M., others, 2023. Monitoring and modelling marine zooplankton in a changing
628 climate. *Nature Communications* 14, 564.

629 Repolho, T., Duarte, B., Dionísio, G., Paula, J.R., Lopes, A.R., Rosa, I.C., Grilo, T.F., Caçador, I., Calado,
630 R., Rosa, R., 2017. Seagrass ecophysiological performance under ocean warming and acidification.
631 Scientific Reports 7, 41443.

632 Roca, M., Dunbar, M.B., Román, A., Caballero, I., Zoffoli, M.L., Gernez, P., Navarro, G., 2022. Monitoring
633 the marine invasive alien species *rugulopteryx okamurae* using unmanned aerial vehicles and satellites.
634 Frontiers in Marine Science 9. <https://doi.org/10.3389/fmars.2022.1004012>

635 Román, A., Tovar-Sánchez, A., Olivé, I., Navarro, G., 2021. Using a UAV-mounted multispectral camera
636 for the monitoring of marine macrophytes. Frontiers in Marine Science 1225.

637 Rossiter, T., Furey, T., McCarthy, T., Stengel, D.B., 2020. UAV-mounted hyperspectral mapping of
638 intertidal macroalgae. Estuarine, Coastal and Shelf Science 242, 106789.

639 Schibalski, A., Kleyer, M., Maier, M., Schröder, B., 2022. Spatiotemporally explicit prediction of future
640 ecosystem service provisioning in response to climate change, sea level rise, and adaptation strategies.
641 Ecosystem Services 54, 101414. <https://doi.org/https://doi.org/10.1016/j.ecoser.2022.101414>

642 Schneider, C.A., Rasband, W.S., Eliceiri, K.W., 2012. NIH image to ImageJ: 25 years of image analysis.
643 Nature methods 9, 671–675.

644 Schreyers, L., Emmerik, T. van, Biermann, L., Le Lay, Y.-F., 2021. Spotting green tides over brittany from
645 space: Three decades of monitoring with landsat imagery. Remote Sensing 13.
646 <https://doi.org/10.3390/rs13081408>

647 Slaton, M.R., Raymond Hunt Jr., E., Smith, W.K., 2001. Estimating near-infrared leaf reflectance from leaf
648 structural characteristics. American Journal of Botany 88, 278–284.
649 <https://doi.org/https://doi.org/10.2307/2657019>

650 Soissons, L.M., Haanstra, E.P., Van Katwijk, M.M., Asmus, R., Auby, I., Barillé, L., Brun, F.G., Cardoso,
651 P.G., Desroy, N., Fournier, J., others, 2018. Latitudinal patterns in european seagrass carbon reserves:

652 Influence of seasonal fluctuations versus short-term stress and disturbance events. *Frontiers in Plant Science*
653 9, 88.

654 Sousa, A.I., Santos, D.B., Silva, E.F. da, Sousa, L.P., Cleary, D.F., Soares, A.M., Lillebø, A.I., 2017. 'Blue
655 carbon' and nutrient stocks of salt marshes at a temperate coastal lagoon (ria de aveiro, portugal). *Scientific*
656 *reports* 7, 41225.

657 Sousa, A.I., Silva, J.F. da, Azevedo, A., Lillebø, A.I., 2019. Blue carbon stock in *zostera noltei* meadows
658 at ria de aveiro coastal lagoon (portugal) over a decade. *Scientific reports* 9, 14387.

659 Sutton, M.A., Van Grinsven, H., Billen, G., Bleeker, A., Bouwman, A., Oenema, O., 2011. European
660 nitrogen assesement-summary for policy makers, in: *The European Nitrogen Assessment. Sources, Effects*
661 *and Policy Perspectives*. pp. xxiv–xxxiv.

662 Tallam, K., Nguyen, N., Ventura, J., Fricker, A., Calhoun, S., O'Leary, J., Fitzgibbons, M., Robbins, I.,
663 Walter, R.K., 2023. Application of deep learning for classification of intertidal eelgrass from drone-
664 acquired imagery. *Remote Sensing* 15, 2321.

665 Traganos, D., Reinartz, P., 2018. Mapping mediterranean seagrasses with sentinel-2 imagery. *Marine*
666 *Pollution Bulletin* 134, 197–209. <https://doi.org/10.1016/j.marpolbul.2017.06.075>

667 Tuyá, F., Hernandez-Zerpa, H., Espino, F., Haroun, R., 2013. Drastic decadal decline of the seagrass
668 *cymodocea nodosa* at gran canaria (eastern atlantic): Interactions with the green algae *caulerpa prolifera*.
669 *Aquatic Botany* 105, 1–6.

670 Unsworth, R.K., Cullen-Unsworth, L.C., Jones, B.L., Lilley, R.J., 2022. The planetary role of seagrass
671 conservation. *Science* 377, 609–613.

672 Veettil, B.K., Ward, R.D., Lima, M.D.A.C., Stankovic, M., Hoai, P.N., Quang, N.X., 2020. Opportunities
673 for seagrass research derived from remote sensing: A review of current methods. *Ecological Indicators* 117,
674 106560.

675 Villalobos Perna, P., Di Febbraro, M., Carranza, M.L., Marzialetti, F., Innangi, M., 2023. Remote sensing
676 and invasive plants in coastal ecosystems: What we know so far and future prospects. *Land* 12, 341.

677 Villares, R., Puente, X., Carballeira, A., 1999. Nitrogen and phosphorus in *Ulva* sp. In the galician rias bajas
678 (northwest Spain): Seasonal fluctuations and influence on growth. *Boletín-Instituto Español de*
679 *Oceanografía* 15, 337–342.

680 Wang, Z., Fang, Z., Liang, J., Song, X., 2022. Assessment of global habitat suitability and risk of ocean
681 green tides. *Harmful Algae* 119, 102324.

682 Wei, P., Lu, Z., Song, J., 2015. Variable importance analysis: A comprehensive review. *Reliability*
683 *Engineering and System Safety* 142, 399–432. [https://doi.org/https://doi.org/10.1016/j.ress.2015.05.018](https://doi.org/10.1016/j.ress.2015.05.018)

684 Xu, S., Xu, S., Zhou, Y., Yue, S., Zhang, X., Gu, R., Zhang, Y., Qiao, Y., Liu, M., 2021. Long-term changes
685 in the unique and largest seagrass meadows in the Bohai Sea (China) using satellite (1974–2019) and sonar
686 data: Implication for conservation and restoration. *Remote Sensing* 13, 856.

687 Ye, N., Zhang, X., Mao, Y., Liang, C., Xu, D., Zou, J., Zhuang, Z., Wang, Q., 2011. “Green tides” are
688 overwhelming the coastline of our blue planet: Taking the world’s largest example. *Ecological Research*
689 26, 477–485.

690 Zoffoli, M.L., Gernez, P., Godet, L., Peters, S., Oiry, S., Barillé, L., 2021. Decadal increase in the ecological
691 status of a north-atlantic intertidal seagrass meadow observed with multi-mission satellite time-series.
692 *Ecological Indicators* 130, 108033. <https://doi.org/10.1016/j.ecolind.2021.108033>

693 Zoffoli, M.L., Gernez, P., Oiry, S., Godet, L., Dalloyau, S., Davies, B.F.R., Barillé, L., 2022. Remote
694 sensing in seagrass ecology: Coupled dynamics between migratory herbivorous birds and intertidal
695 meadows observed by satellite during four decades. *Remote Sensing in Ecology and Conservation*.
696 <https://doi.org/10.1002/rse2.319>

697 Zoffoli, M.L., Gernez, P., Rosa, P., Le Bris, A., Brando, V.E., Barillé, A.-L., Harin, N., Peters, S., Poser,
698 K., Spaias, L., Peralta, G., Barillé, L., 2020. Sentinel-2 remote sensing of zostera noltei-dominated intertidal
699 seagrass meadows. Remote Sensing of Environment 251, 112020.
700 <https://doi.org/https://doi.org/10.1016/j.rse.2020.112020>